

Detection of non-Gaussianity in the WMAP 1-year data
using spherical wavelets

P. Vielva¹, E. Martínez-González¹, R. B. Barreiro¹, J. L. Sanz¹ and L. Cayon^{1;2}

(1) Instituto de Física de Cantabria, Fac. de Ciencias, Av. de los Castros s/n,
39005-Santander, Spain

(2) Department of Physics, Purdue University, 525 Northwestern Avenue, West Lafayette, IN
47907-2036, USA

A B S T R A C T

A non-Gaussian detection in the WMAP 1-year data is reported. The detection has been found in the combined $Q-V-W$ WMAP proposed by the WMAP team (Komatsu et al. 2003) after applying a wavelet technique based on the Spherical Mexican Hat Wavelet (SMHW). The skewness and the kurtosis of the SMHW coefficients are calculated at different scales (ranging from a few arcmins to tens of degrees). A non-Gaussian signal is detected at scales of the SMHW around 4° (size in the sky of around 10°). The significance of this detection is 99.9% . In addition a study of Gaussianity is performed in each hemisphere. The northern hemisphere is compatible with Gaussianity, whereas the southern one deviates from Gaussianity at a significance level $> 99.9\%$. Systematics and foregrounds are carefully studied in order to identify the possible source of non-Gaussianity. Contribution from systematic effects (related to noise and beams) is rejected: 1) each one of the Q , V and W maps shows the same non-Gaussianity pattern, and 2) several combinations of the different receivers at each band (that highly reduce the CMB and the foreground emissions) do not show this non-Gaussian pattern. Similarly, the Galactic foregrounds do not contribute significantly to the non-Gaussian detection: non-Gaussianity is detected in all the WMAP maps (from 23 GHz to 94 GHz) and no frequency dependence is observed. Moreover, the expected foreground contribution to the combined WMAP map was added to CMB Gaussian simulations showing a behaviour compatible with the Gaussian model. Hence, possible intrinsic temperature fluctuations (like secondary anisotropies and primordial features) can not be rejected as the source of this non-Gaussian detection. We remark that our result implies not only asymmetries north/south (like other previous WMAP analyses) but also a direct non-Gaussian detection.

Subject headings: methods: data analysis {cosmic microwave background

⁰ e-mail: vielva@ifica.unican.es

1. Introduction

The study of the Gaussianity of the Cosmic Microwave Background (CMB) is one of the most powerful mechanisms for understanding the nature of the primordial density fluctuations: by measuring the probability distribution of the temperature fluctuations of the CMB, several models for the primordial density fluctuations can be rejected or accepted at a certain confidence level. For instance, standard inflationary models predict that the temperature fluctuations of the CMB correspond to a Gaussian, homogeneous and isotropic random field; whereas non-standard inflation (Linde & Mukhanov 1997, Peebles 1997, Benardeau & Uzan 2002 and Acquaviva et al. 2002) and topological defects models (Turk & Spergel 1990 and Durrel 1999) usually predict non-Gaussian random fields. Moreover, the Gaussianity study can also be used as a very useful tool for pointing out secondary anisotropies produced by the reionization of the universe (Ostriker & Vishniac 1986 and Aghanim et al. 1996), the Rees-Sciama effect due to the non-linear evolution of the large scale structure (Rees & Sciama 1968 and Martinez-Gonzalez & Sanz 1990), gravitational lensing (Martinez-Gonzalez et al. 1997, Hu 2000 and Goldberg & Spergel 1999)... One of the handicaps within the detection of non-Gaussian signatures is related to the contamination of the CMB signal due to foregrounds (like the Galactic emissions and the compact sources). These components produce spurious non-Gaussian signals that can contaminate any intrinsic signature.

In order to distinguish and constrain the nature of the primordial density fluctuations (or to conclude that the anisotropies are secondary), it is essential to have high-resolution, low-noise and large-coverage CMB data. Recently, the Wilkinson Microwave Anisotropy Probe (WMAP) NASA satellite has reported the 1-year all-sky data (Bennet et al. 2003a). The WMAP science team (Komatsu et al. 2003) found the data to be consistent with Gaussianity. Two statistics were used: a measure of the phase correlations of temperature fluctuations (taking into account all the combinations of the bispectrum) and the Minkowski functionals; moreover, improved limits for the non-linear coupling parameter were established. Other groups have presented different analyses of Gaussianity on WMAP: Colley & Gott (2003) have done an independent genus topology (one of the three Minkowski functionals) study, by performing a stereographic projection of the WMAP data, finding also Gaussian compatibility. Chiang et al. (2003) presented a Gaussianity study of the CMB map obtained from the WMAP data by Tegmark et al. (2003) using a Wiener Filter technique; a statistic based on the random-phase hypothesis is used. They found a significant non-Gaussian contribution at high multipoles. The authors conclude that the found non-Gaussianity is due to unremoved foreground contamination. Gaztanaga & Wagg (2003) have performed a 3-point angular correlation function analysis, finding good agreement with the Gaussian hypothesis and bounding the non-linear coupling parameter. Higher-order moments (up to six) of the angular correlation function were calculated by Gaztanaga et al. (2003) which show the same Gaussian agreement. Another genus-statistic study has been done by Park (2003) using the foreground cleaned frequency maps of the WMAP data; a stereographic projection is also used finding a non-Gaussian detection by comparing the difference of the negative and positive genus (with respect to the Gaussian prediction) at different threshold levels. Several sources are considered in order to

explain this detection, but higher signal-to-noise ratio data is needed to distinguish among them. Eriksen et al. (2003) have computed 2- and 3-point correlations finding north/south asymmetries in the WMAP data. These asymmetries appear at large and intermediate scales and are associated with a lack of structure in the northern hemisphere, while the southern one is compatible with the Gaussian model (additional asymmetries east/west are also found).

In this work we present a wavelet analysis of the Gaussianity of the WMAP 1-year all-sky map performed in wavelet space. Wavelets have been extensively used in the analysis of the CMB data, not only concerning Gaussianity studies, but also in the component separation field (Tenorio et al. 1999, Cayon et al. 2001, Vielva et al. 2001a, Vielva et al. 2001b, Vielva et al. 2003 and Stolyarov et al. 2003) and in denoising techniques (Sanz et al. 1999a,b). Regarding the application of wavelets to Gaussianity studies, Hobson et al. (1999) have shown that the wavelet coefficients provide a significantly better detection of non-Gaussian features due to cosmic strings than the Minkowski functionals. Similarly, Aghanim et al. (2003) have shown that the wavelet space is more efficient to detect non-Gaussian features than other typical estimators like those based in Fourier analysis (bispectrum and trispectrum). Even more, due to the special nature of wavelets, the non-Gaussian sources can not only be detected but also identified in the maps, since the spatial information is kept in the wavelet space. Moreover, as it was shown in Barreiro & Hobson (2001) and in Martínez-González et al. (2002), the optimal combination of the information given by the wavelet coefficients at different scales, highly increases the power of wavelets to detect weak non-Gaussian signals.

The first application of wavelet techniques to detect non-Gaussian signatures was done by Pando et al. (1998), where the 2D *à la* Daubechies-4 wavelet was used to analyse the COBE-DMR data (see Mukherjee et al. 2000 for a critical review of this work). Lately, several works have used wavelets to study the Gaussianity of the COBE-DMR maps in the HEALPix scheme (Gorski et al. 1999): Barreiro et al. (2000) have used the Spherical Haar Wavelet (SHW), whereas Cayon et al. (2001, 2003) have used the Spherical Mexican Hat Wavelet (SMHW). A critical comparison between the performances of both spherical wavelets for detecting non-Gaussian features (skewness and kurtosis) was done by Martínez-González et al. (2002).

The aim of this paper is to apply the technique developed in Cayon et al. (2001) and Martínez-González et al. (2002) to the 1-year all-sky WMAP data in order to detect non-Gaussian features. It is organized as follows. In Section 2 the process to generate the simulations and to reduce the data is explained. In Section 3 the SMHW is briefly described and the different statistics are defined. The SMHW analysis is presented in Section 4, and the possible sources of the detected non-Gaussianity are discussed in Section 5. Finally the conclusions are given in Section 6.

2. The WMAP data reduction and WMAP-like simulations

The NASA Wilkinson Microwave Anisotropy Probe (WMAP) satellite was launched in the summer of 2001 and in February 2003 the 1-year results were presented. The WMAP radiometers

observe at 5 frequency bands: K-band (22.8 GHz, 1 receiver), Ka-Band (33.0 GHz, 1 receiver), Q-Band (40.7 GHz, 2 receivers), V-Band (60.8 GHz, 2 receivers) and W-Band (93.5 GHz, 4 receivers). All the papers, data and products generated by the WMAP team can be found in the Legacy Archive for Microwave Background Data Analysis (LAMBDA) webpage¹. The noise and beam properties can be also found in the LAMBDA webpage. The WMAP maps are presented in the Hierarchical, Equal Area and iso-Latitude Pixelization (HEALPIX, Gorski et al. 1999) at the $N_{\text{side}} = 512$ resolution parameter. The number of pixels is given by $12N_{\text{side}}^2$.

In order to perform the Gaussianity study, the WMAP team (Komatsu et al. 2003) suggests to combine all the maps produced by the receivers where the CMB is the dominant signal (Q-Band, V-Band and W-Band). We have followed the recommendation given by the WMAP team in the choice of the combined map used in the analysis. We would like to point out that no previous work in the literature regarding studies of Gaussianity of the WMAP data has analysed the same combined map proposed by the WMAP team (except the one performed by the WMAP team itself).

A very simple pipeline is given in Bennett et al. (2003b). At a given position in the sky (\mathbf{x}), the temperature is given by:

$$T(\mathbf{x}) = \frac{\sum_{j=3}^{10} T_j(\mathbf{x}) w_j(\mathbf{x})}{\sum_{j=3}^{10} w_j(\mathbf{x})}; \quad (1)$$

where the index $j = 3;4$ is for the Q-Band receivers, $j = 5;6$ for the V-Band ones and $j = 7;8;9;10$ for the W-Band (the index $j = 1;2$ corresponds to the K and Ka receivers, respectively). The noise weight $w_j(\mathbf{x})$ is defined by:

$$w_j(\mathbf{x}) = \frac{N_j(\mathbf{x})}{\sigma_j^2} \quad (2)$$

where σ_j is the noise dispersion per observation and $N_j(\mathbf{x})$ is the number of observations made by receiver j at the position \mathbf{x} (see Bennett et al. 2003a). Equation (1) provides a single map where the signal-to-noise has been increased. Although the CMB dominated frequencies have been chosen, we still have significant contribution due to Galactic foregrounds (thermal dust, free-free and synchrotron) as well as extragalactic point sources (negligible Sunyaev-Zel'dovich contribution is expected, see Bennett et al. 2003b). In order to avoid the Galactic emissions, the WMAP team performed a foreground template \hat{t} described in Section 6 of Bennett et al. 2003b. The 94 GHz dust map of Finkbeiner et al. (1999) is used as the thermal dust template; the H α map of Finkbeiner (2003) corrected for extinction through the E_{B-V} map of Schlegel et al. (1998) is used as the free-free template; finally, the synchrotron template is the 408 MHz Haslam et al. (1982) map. Hence, Equation (1) is modified by:

$$\hat{T}(\mathbf{x}) = \frac{\sum_{j=3}^{10} \hat{T}_j(\mathbf{x}) w_j(\mathbf{x})}{\sum_{j=3}^{10} w_j(\mathbf{x})}; \quad (3)$$

¹<http://cmbdata.gsfc.nasa.gov/>

where $\hat{T}_j(\mathbf{x})$ is the temperature at position \mathbf{x} for the receiver j after foreground correction. The parameters for the best-fit of the foreground templates are given in Bennett et al. (2003b). Even more, the foreground cleaned frequency maps can be found in the LAMBDA site.

Laterly, the map is degraded to resolution $N_{\text{side}} = 256$ (since the very small scales are dominated by noise) and a mask is applied to avoid the contamination due to the strong emission at the Galactic plane and the contribution due to known radio point sources. This mask is called Kp0 and can also be found in the LAMBDA site (it is the most conservative mask of the 3 ones proposed by the WMAP team). Finally, the residual monopole and dipole outside the mask are removed. The final map is shown in Figure 1.

In order to study the Gaussianity of this map, we have produced 1000 Gaussian simulations. Using CMBFAST (Seljak & Zaldarriaga 1996), we calculated the C_ℓ given by the cosmological parameters estimated by WMAP team (Table 1 of Spergel et al. 2003). Random Gaussian $a_{\ell m}$ of CMB realizations are calculated and convolved at each one of the WMAP receivers with the adequate beams (provided in the LAMBDA site). After the transformation from the harmonic to real space, noise realizations have been added following the number of observation per pixel ($N_j(\mathbf{x})$) and the noise dispersion per observation (σ_j). We have combined all the maps following Equation (3). Finally, the Kp0 mask was applied, the 1000 simulations are degraded to $N_{\text{side}} = 256$ and the residual monopole and dipoles were subtracted.

3. The tool and the non-Gaussian estimators

Without any doubt, wavelet techniques are one of the most powerful tools for the detection of non-Gaussianity in CMB data (Hobson et al. 1999, Aghanim et al. 2003). Due to the special nature of wavelets, a multi-scale study can be performed, allowing the amplification of those non-Gaussian features that dominate at a given scale. Moreover, the SMHW is ideal for the enhancement of non-Gaussian signatures with spherical symmetry. The SMHW has been already applied for non-Gaussian studies to the COBE-DMR data (Cayon et al. 2001, 2003) and to Planck simulations (Martinez-Gonzalez et al. 2002). The SMHW can be obtained from the euclidean Mexican Hat Wavelet (MHW) following the stereographic projection suggested by Antoine & Vanderheynt (1998). This projection assures that the wavelet properties are kept as well as the recovery of the MHW at the small angle limit (see Martinez-Gonzalez et al. 2002 for a graphical explanation of this extension). The SMHW satisfies the compensation, admissibility and normalization properties that define a wavelet, and it is given by:

$$s(y;R) = \frac{1}{2 N(R)} \left[1 + \left(\frac{y}{2}\right)^2 \right]^{-2} \left(\frac{y}{R}\right)^2 e^{-y^2/2R^2}; \quad (4)$$

where R is the scale and $N(R)$ is a normalization constant:

$$N(R) = R \left[1 + \frac{R^2}{2} + \frac{R^4}{4} \right]^{-1/2}; \quad (5)$$

The distance on the tangent plane is given by y that is related to the polar angle (θ) through:

$$y = 2 \tan \frac{\theta}{2} \tag{6}$$

At a given scale (R) , several statistics can be defined. In this work we have used two simple non-Gaussian estimators: skewness $(S(R))$ and kurtosis $(K(R))$:

$$S(R) = \frac{1}{N_R} \sum_{i=1}^{N_R} w_i(R)^3 \cdot (R)^3 \tag{7}$$

$$K(R) = \frac{1}{N_R} \sum_{i=1}^{N_R} w_i(R)^4 \cdot (R)^4; \tag{8}$$

where (R) is the dispersion of the wavelet coefficients at the scale R $(w_i(R))$:

$$(R)^2 = \frac{1}{N_R} \sum_{i=1}^{N_R} w_i(R)^2; \tag{9}$$

In the previous $S(R)$, $K(R)$ and (R) definitions, it is assumed that the N_R wavelet coefficients $(w_i(R))$ have zero mean at each scale R .

4. The Spherical Wavelet analysis

In order to test the Gaussianity of the WMAP 1-year data, we have applied the following analysis using the SMHW.

First, we have performed 1000 simulations following the pipeline proposed by Bennett et al. (2003b) and already indicated in Section 2. Each one of these simulations have been convolved with the SMHW at different scales ($R_1 = 13.7, R_2 = 25.0, R_3 = 50.0, R_4 = 75.0, R_5 = 100.0, R_6 = 150.0, R_7 = 200.0, R_8 = 250.0, R_9 = 300.0, R_{10} = 400.0, R_{11} = 500.0, R_{12} = 600.0, R_{13} = 750.0, R_{14} = 900.0, R_{15} = 1050.0, R_{16} = 1200.0, R_{17} = 1350.0, R_{18} = 1500.0$ and $R_{19} = 3600.0$ arcmin). These simulations help to establish different confidence limits (e.g., 68%, 95% and 99%) at each scale. Second, the same analysis is applied to the WMAP map $(\hat{T}(x))$ represented in Figure 1. The results of this analysis are shown in Figure 2: neither the skewness nor the kurtosis deviates strongly from Gaussianity. However, as can be clearly seen, the kurtosis is above the 95% confidence level at scales around R_8 .

Since we are convolving a map with a large Galactic mask plus known point sources (the so-called kp0 one) with the SMHW, we are introducing in the wavelet analysis a large number of pixels {those near the border of the mask} very affected by the zero value of the mask. This effect is taken into account through the simulations, but, obviously, it is introducing an undesirable loss of efficiency. In order to avoid this effect, we will not consider pixels whose SMHW coefficients have

a strong contamination due to the mask. In other words, we exclude these pixels after the SMHW convolution. Since we are convolving the combined WMAP map ($\hat{\Gamma}(x)$) with different scales, the number of pixels to be excluded is growing with the scale. There could be several criteria to define this set of exclusion masks. We have tested several definitions and all of them lead to the same results. The results here presented were obtained with an exclusion mask defined as follows: at a given scale (R), the exclusion mask $M(R)$ is composed by the Kp0 mask plus those pixels that are closer than $2.5R$ to any one of the pixels of the Kp0 mask that are nearby the Galactic plane. In other words, at a given scale, the exclusion mask is an enlargement (proportional to the scale) of the Kp0 mask from the Galactic plane (but note that the mask is not increased around the masked point sources). Because this enlargement of the Kp0 mask from the Galactic plane as a function of the scale, the four largest SMHW scales ($R_{16} = 1200.0$, $R_{17} = 1350.0$, $R_{18} = 1500.0$ and $R_{19} = 3600.0$ arcmin) are not used, since almost all the sky is excluded for the analysis. The exclusion mask corresponding to the remaining 15 scales is plotted in Figure 3.

We have repeated the SMHW analysis considering only those pixels outside the exclusion mask at each scale. Results are presented in Figure 4: an excess of kurtosis is detected at three consecutive scales: $R_7 = 3.33$, $R_8 = 4.17$ and $R_9 = 5$. The three values for the kurtosis are now non-Gaussian detections above 99%. The three scales are correlated. Using the simulations, we can establish a combined confidence level for this detection, by determining the number of Gaussian simulations that can produce a non-Gaussian signal above the one detected. Only one Gaussian simulation shows values for the kurtosis at the R_7 , R_8 and R_9 scales above the values given by the WMAP data. Hence, our non-Gaussian detection has a very strong confidence level of 99.9%. We want to remark that this value is obtained for very different definitions of the exclusion mask. For instance, we have tested an enlargement of the Kp0 mask from the Galactic plane scaling with the SMHW scale (R) as: $0.7R$, $0.8R$, $0.9R$, $1.0R$ and 1.75 . Even more, an enlargement of the whole Kp0 mask (not only from the Galactic Plane but also from all the masked point sources) has been also checked given quite similar results.

In addition we have performed the SMHW analysis in each hemisphere to determine if the non-Gaussian detection is present in all the sky. Previous non-Gaussian works on the WMAP data have reported some asymmetries between the northern and the southern hemisphere (Park 2003, Eriksen et al. 2003). As Figure 5 clearly shows, the kurtosis is located in the southern hemisphere. The non-Gaussian detection in the southern hemisphere occurs at the $R_6 = 2.50$; $R_7 = 3.33$ and $R_8 = 4.17$ SMHW scales, being all of them above the 99% confidence level. Only one simulation presents values for the kurtosis equal or larger than the detected ones at those scales. Hence, the confidence level for this detection is, again the 99.9%. Even more, since the R_9 scale is almost above the 99% confidence level, we can also include this scale in order to define the significance level. None of the 1000 simulations is above the kurtosis curve for the R_6 , R_7 , R_8 and R_9 scales. Hence, we can conclude that the significance level for the kurtosis detection at the southern hemisphere is $> 99.9\%$.

By looking at the scalogram of the wavelet coefficients in the northern and southern hemi-

spheres (dispersions at the different scales R in Figure 5), we can see that the northern hemisphere shows less structure than the southern one, at scales between 4 and 12. On the other hand, the northern hemisphere has more structure than the southern one at larger scales. However, the scalogram of both hemispheres are within the confidence level of the Gaussian model.

Let us remark that, as mentioned before, previous works have reported asymmetries between the northern and southern hemispheres. For instance, Park (2003) has found a different north/south genus behaviour which implies a non-Gaussian detection at the 99%. Eriksen et al. (2003) also find an asymmetric behaviour north/south regarding the structure level at large and intermediate angular scales: the northern hemisphere has a lack of structure whereas the southern one is compatible with the Gaussian model. However, our study reveals: 1) a direct measurement of non-Gaussian signatures related to the kurtosis of those structures with a typical size in the sky of around 10, with a significance 99.9%; 2) the southern hemisphere shows an excess of kurtosis with a significance $> 99.9\%$ (around the previous scale) whereas the northern one is compatible with the Gaussian model.

As a proof of the robustness of the non-Gaussianity detection, we have repeated the whole analysis by performing (previously to the SMHW convolution) a whitening of the a_m of both, the data and the simulations. This whitening minimises any possible errors in the estimation of the C_ℓ of the Gaussian model and it proves that our detection corresponds to non-Gaussian features present in the phases of the harmonic coefficients.

Finally, we want to remark that we have performed also a wavelet analysis based on the Spherical Haar Wavelet (SHW) as it was proposed in Martínez-González et al. (2002). We did not find any non-Gaussian detection using the SHW. This is not so surprising, since (as it was shown in Martínez-González et al., 2002) the SHW is less efficient than the SMHW to detect non-Gaussian signals.

5. Discussion: Sources of non-Gaussianity

The detection of non-Gaussianity in the WMAP map $\hat{T}(\mathbf{x})$ was presented in the previous Section. The kurtosis of the wavelet coefficients at scales $R = 4$ has a very high significance of 99.9% being localized in the southern hemisphere.

The aim of this Section is to study, as far as we can, the source of this non-Gaussianity. We look for the possible influence of some systematic effects (is any of the receivers the responsible of the detection?, or the noise?, or the beam?). This is investigated in Subsection 5.1. In Subsection 5.2 we present tests to study the possible influence of the Galactic foregrounds in the detection (the brightest point sources are masked in the kp0 mask and the contribution of the Sunyaev-Zeldovich effect is almost negligible, see Bennett et al. 2003b) in Subsection 5.2.

Finally, in Subsection 5.3, we speculate with intrinsic fluctuations as a possible reason for this

detection.

5.1. Is it due to Systematics?

Our first test to check the influence of systematics in the non-Gaussian detection consists in looking for any rare channel. Instead of analysing the WMAP map $\hat{T}(x)$ obtained by the weighted average of all the Q-Band, V-Band and W-Band receivers, we perform the SMHW analysis in each frequency map $\hat{T}_Q(x)$, $\hat{T}_V(x)$ and $\hat{T}_W(x)$ independently. If the results are the same for these combinations, then we can conclude that the detection of non-Gaussianity is not produced by a particular channel. Results are presented in Figure 6 (left panel). The $K(R)$ curve obtained for the WMAP map $\hat{T}(x)$ is plotted together with the curves obtained for $K_Q(R)$, $K_V(R)$, $K_W(R)$. The confidence levels for the WMAP map $\hat{T}(x)$ given by the Gaussian simulations are also plotted for a better comparison. We can see how the pattern for the $K(R)$ curve is followed almost perfectly by the other kurtosis curves.

We have also checked for the influence of systematics related with instrumental features (noise and beams). We performed the SMHW analysis on maps produced from the subtraction of receivers at the same frequency. These maps are almost free from CMB and foreground contribution (remaining residuals can be present due to the slightly different resolutions between the two subtracted channels). In particular, we have analysed the maps obtained by subtracting the two receivers in the Q-band ($Q_1 - Q_2$), the two receivers in V-Band ($V_1 - V_2$) and the map obtained from $W_1 - W_2 + W_3 - W_4$. As can be seen in Figure 6 (right panel), the patterns followed by the kurtosis in these three cases are completely different from the $K(R)$ curve obtained for the WMAP map $\hat{T}(x)$. A gain, the confidence regions for the WMAP map $\hat{T}(x)$ have been plotted for a better comparison and thus it is not surprising that the kurtosis at some scales in the difference maps appears outside the confidence regions. Those patterns are probably due to the resulting noise at each frequency band (for instance, we have checked with simulations that only the noise can explain that behaviour for the combined $Q_1 - Q_2$ map).

Hence, these tests seem to indicate that systematic effects have not a significant role in the non-Gaussian signature.

5.2. Is it due to Foregrounds?

Foregrounds have been considered as the next possible source of non-Gaussianity. We only care about the Galactic foregrounds because the brightest radio sources have been previously masked (moreover, the angular scale of the non-Gaussian detection is much larger than the WMAP angular resolution) and the expected Sunyaev-Zeldovich effect contribution is almost negligible (Bennett et al. 2003b).

The left panel of Figure 6 is very useful. It shows a constant frequency dependence for the non-Gaussian detection: for the frequency range of Q, V and W (from 41 GHz to 94 GHz), the found non-Gaussian pattern for the kurtosis does not resemble any of the frequency dependence due to the Galactic foregrounds (synchrotron, free-free and thermal dust).

At this point, we remark that, if the K and Ka channels are analysed, the pattern for the kurtosis curve does not follow completely the one for the other WMAP channels. Whereas the peak around R_8 clearly appears, the behaviour is very different at scales below R_6 . In addition, there is an offset along all the scales. We think that this effect corresponds with the very high foreground contamination that these channels show. In order to clarify this, we have done the following exercise. We have generated an additional CMB map by subtracting the Ka map (at 33 GHz) from the K one (at 23 GHz), multiplying the first one by a factor of 2.65. This number corresponds to the expected increment of the synchrotron emission from 33 GHz to 23 GHz². As it can be seen in Figure 7, the pattern of the kurtosis curve is the same than the one detected for the combined WMAP map ($\hat{T}(x)$) (the confidence regions for this last map have been plotted again for comparison). Therefore, the same pattern for the kurtosis is found, not only for the Q, V and W bands, but also for the whole WMAP frequency range (from 23 GHz to 94 GHz). This implies not only that the synchrotron does not seem to be the source for the non-Gaussian signature, but also that this detection does not show any significant frequency dependence. An additional test to check the influence of the foregrounds was done by analysing a map where the CMB contribution is small: the two receivers of the Q-Band and the two ones of the V-Band are subtracted from the four receivers of the W-Band. In this map we have significant contributions from the foregrounds and the noise. The SMHW analysis of this map also shows (Figure 8) that, apparently, the foregrounds are not the source for the non-Gaussian detection, since the pattern of the kurtosis curve is completely different from the one estimated from the combined WMAP map ($\hat{T}(x)$).

Finally, we have done the following exercise. We have estimated the foreground correction ($F(x)$) subtracted from the data by the WMAP team just by doing: $F(x) = T(x) - \hat{T}(x)$. This foreground correction is added to a Gaussian simulation of the combined WMAP map. The SMHW analysis was performed in this contaminated map. As shown in Figure 9, the curve for the kurtosis ($K(R)$) not only has a pattern completely different from the one detected in the combined WMAP map ($\hat{T}(x)$) but is also totally compatible with the Gaussian simulations. Even more, the foreground correction ($F(x)$) was added twice to the Gaussian simulation, finding the same behaviour. This exercise (as the previous ones) also seems to discard the foreground emissions as the one responsible for the non-Gaussian detection.

²A power law is assumed for the frequency dependence of the synchrotron emission: $T_{\text{syn}}(\nu) / T_{\text{syn}}(\nu_0) = (\nu / \nu_0)^{2.7}$, as it was proposed by Bennet et al. (2003b).

5.3. Is it due to Intrinsic fluctuations?

The two previous Subsections have shown that there are not strong evidences for the non-Gaussian detection due to neither systematic effects nor Galactic foreground emissions. Therefore, other sources for this detection may be considered. In particular, intrinsic fluctuations can not be rejected at all.

One of the powerful advantages of the wavelet analysis is the possible identification, on the sky, of the non-Gaussian source. In Figure 10 (left panel) the SMHW coefficient at the scale R_8 are plotted. The minimum value of this map is $4.57 (R_8)$, where (R_8) is the dispersion of the wavelet coefficients at scale R_8 . Using the Gaussian simulations, we have checked that the probability for an extremum like this is 1% . The right panel of Figure 10 shows those SMHW coefficients that are above (in absolute values) $3 (R_8)$. If these pixels are not taken into account in the kurtosis calculation, the estimation for this statistic is perfectly compatible with the Gaussian simulations (within the 68% confidence region).

A very interesting exercise was done in order to study the previous very cold spot (in SMHW space) in the southern hemisphere ($l = 57^\circ; b = 209^\circ$). We have calculated the mean value of the cold spot at each one of the WMAP frequency channels. As shown in Figure 11, the frequency dependence of this spot follows the CMB one, and is not compatible with any of the Galactic foregrounds. Notice that if the 2.68 times Ka map is subtracted from the K one, we get an even better agreement with a constant frequency dependence, given by the dot-dashed line. We have also studied the frequency dependence of this cold spot in real space (after filtering all the frequency maps with a Gaussian beam of FWHM = $10'$, the size corresponding to the SMHW scale R_8). A good agreement with the CMB behaviour is found for bands Q, V and W, whereas a clear contamination due to synchrotron appears between bands K and Ka. However, when the 2.68 times Ka map is subtracted from the K one, the CMB behaviour is recovered. We notice that whereas for the K and Ka bands in real space the synchrotron emission dominates over CMB, this is not the case for K and Ka bands in wavelet space, since the SMHW has diminished the synchrotron amplitude relative to the CMB one (due to the large scale variation of the former).

Hence, the frequency analysis performed on the cold spot, also indicates that the foregrounds do not seem to be the source of the non-Gaussianity detection.

There are several possibilities which can explain the non-Gaussian detection for the kurtosis of the SMHW coefficients. For instance, massive superstructures (like superclusters or Great Attractor-like structures) or large voids, can produce secondary anisotropies through the Rees-Sciama effect (Martinez-Gonzalez & Sanz 1990). Even more, also primordial anisotropies can be considered. Non standard inflationary models could also explain the detected non-Gaussianity (see e.g. Acquaviva et al. 2002 and references therein). In addition, some kind of topological defects like monopoles or textures (Turok & Spergel 1990) could be present in the sky. On the contrary, non isotropic topological defects like cosmic strings may not produce this kind of non-Gaussianity, since their characteristic scale is around arcminutes and also the detection has been done with an

isotropic wavelet.

6. Conclusions

We have presented the detection of non-Gaussianity in the WMAP 1-year data, in the kurtosis of the SMHW coefficients at scales around 4° , which implies a size in the sky of around 10° . The confidence level of this detection is 99.9%. The Gaussianity study was also done on both hemispheres independently, showing that the northern hemisphere is compatible with the Gaussian model, whereas the southern one presents a very clear non-Gaussian signal quite similar to the one detected in the all-sky analysis. The southern detection has a significance $> 99.9\%$.

The hemisphere analyses also show that the northern hemisphere seems to have less structure than the southern one at scales between 4° and 12° , whereas the southern one has less structure than the northern hemisphere at larger scales. However, both scalograms, the one for the north and the one for the south, seem to be compatible with the Gaussian model. Our non-Gaussian detection differs from other asymmetries reported up to date (Park 2003 and Eriksen et al. 2003), since a direct non-Gaussian signature has been found in the kurtosis of the wavelet coefficients at scale $R \approx 10^\circ$.

The detection appears by analysing, at each SMHW scale, only those pixels with a small contribution of the Galactic mask ($b < 0$). If this pixel selection is not performed, the non-Gaussian signal is within the 99% confidence region. This is not surprising, since the inclusion of SMHW pixels clearly affected by the mask, decreases the efficiency of the analysis. However, the non-Gaussian detection does not depend on the choice of the pixel selection at all, since we have tested that it appears at the same confidence level for several choices.

The same result is also achieved if the SMHW analysis is done after performing a whitening of the harmonic coefficients. This gives robustness to the result, since possible errors in the estimation of the C_l of the Gaussian model do not affect it.

We have performed several tests in order to identify the source of this non-Gaussian signature. Systematics and foregrounds have been carefully studied. The different channels have been checked, showing that all the CMB dominated ones (Q, V and W) have the same pattern for the kurtosis of the SMHW coefficients. Moreover, by analysing the maps produced by subtracting the data given by the receivers at each frequency (these maps are almost free of CMB and foreground contributions) we have proved that the non-Gaussian signal disappears.

The non-Gaussian signal appears in the whole WMAP frequency range (from 23 GHz to 94 GHz) showing no frequency dependence. This seems to indicate no correlation with foregrounds. Even more, we added overestimated foreground contamination to Gaussian CMB maps, showing that the detected non-Gaussian signal does not appear in the SMHW analysis.

Thanks to the properties of the SMHW, we can identify (in the sky) the possible source of the

non-Gaussianity. We have found a cold spot in the southern hemisphere (in $b = 57^\circ; l = 209^\circ$) with a probability $\sim 1\%$. The frequency dependence for this spot is compatible with the CMB one. Obviously, a more detailed study of extrema is required (this will be done in a future work), but this one gives us an additional information about the non-Gaussianity detection. This study should be done in both real and wavelet spaces and could be very useful in order to clarify if the non-Gaussian signature is localized in certain positions on the sky or otherwise, it is produced by a non-Gaussian temperature distribution.

Finally, taking into account all the performed tests, intrinsic fluctuations (due to secondary anisotropies like the Rees-Sciama effect or due to primordial fluctuations produced by topological defects or non-standard inflation) cannot be rejected. The WMAP 2-year data will be, undoubtedly, very useful to confirm or not these results.

Authors kindly thank Dr. Eiichiro Komatsu for very useful comments regarding the data reduction and suggestions and Julio Edgar Gallegos for useful discussions. PV thanks Universidad de Cantabria (UC) for a postdoc grant. RBB thanks UC and Spanish Ministerio de Ciencia y Tecnología (MCYT) for a Ramón y Cajal contract. We acknowledge partial financial support from the Spanish MCYT project ESP2002-04141-C03-01. We acknowledge the use of the Legacy Archive for Microwave Background Data Analysis (LAMBDA). Support for LAMBDA is provided by the NASA Office of Space Science. This work has used the software package HEALPIX (Hierarchical, Equal Area and iso-latitude pixelization of the sphere, <http://www.eso.org/science/healpix>), developed by K.M. Gorski, E.F. Hillon, B.D. Wandelt, J. Banday, F.K. Hansen and M. Barthelemy. We acknowledge the use of the software package CMBFAST (<http://www.cmbfast.org>) developed by U. Seljak and M. Zaldarriaga.

REFERENCES

- Acuaviva V., Bartolo N., Matarrese S. & Riotto A., 2002, preprint (astro-ph/0209156)
- Aghanim N., Desert F.X., Puget J.L. & Gispert R., 1996, *A & A*, 311, 1
- Aghanim N., Kunz M., Castro P.G. & Fomio., 2003, *A & A*, 406, 797
- Antoine J.P. & Vanderheynt P., 1998, *J. Math Phys.*, 39, 3987
- Barreiro R.B., Hobson M.P., Lasenby A.N., Banday A.J., Gorski K.M. & Hinshaw G., 2000, *MNRAS*, 318, 475
- Barreiro R.B. & Hobson M.P., 2001, *MNRAS*, 327, 813
- Bennett C.L. et al., 2003a, *ApJ*, in press
- Bennett C.L. et al., 2003b, *ApJ*, in press

- Bernardeau F., Uzan J.-P., 2002, *Phys. Rev. D*, 66, 103506
- Cayon L., Sanz J. L., Barreiro R. B., Mart nez{G onzalez E., Vielva P., To olatti L., Silk J., Diego J. M. & Argueso F., 2000, *MNRAS*, 315, 757
- Cayon L., Sanz J. L., Mart nez{G onzalez E., Banday A. J., Argueso F., Gallegos J. E., Gorski K. M. & Hinshaw G., 2001, *MNRAS*, 326, 1243
- Cayon L., Mart nez{G onzalez E., Argueso F., Banday A. J. & Gorski K. M., 2003, *MNRAS*, 339, 1189
- Chiang L.-Y., Naselsky P. D., Verkhodanov O. V. & Way M. J., 2003, *ApJ*, 590, L65
- Colley W. N. & Gott J. R., 2003, preprint (astro-ph/0303020)
- Durrer R., 1999, *New Astron. Rev.*, 43, 111
- Eriksen H. K., Hansen F. K., Banday A. J., Gorski K. M. & Lilje P. B., 2003, preprint (astro-ph/0307507)
- Finkbeiner D. P., Davis M. & Schlegel D. J., 1999, *ApJ*, 524, 867
- Finkbeiner D. P., 2003, *ApJS*, 146, 407
- Gaztanaga E. & Wagg J., 2003, preprint (astro-ph/0305327)
- Gaztanaga E., Wagg J., Multamaki T., Montana A. & Hughes D. H., 2003, preprint (astro-ph/0304178)
- Goldberg D. M. & Spergel D. N., 1999, *Phys. Rev.*, D 59, 103002
- Gorski K. M., Wandelt B. D., Hansen F. K., Hivon E. & Banday A. J., 1999, (astro-ph/9905275)
- Haslam C. G. T., Salter C. J., Sto el H. & Wilson W. E., 1982, *A & A S*, 47, 1
- Hobson M. P., Jones A. W. & Lasenby A. N., 1999, *MNRAS*, 309, 125
- Hu W., 2000, *Phys. Rev.*, D 62, 043007
- Komatsu E. & Spergel D. N., 2001, *Phys. Rev. D*, 63, 063002
- Komatsu E. et al., 2003, *ApJ*, in press
- Linde A. & Mukhanov V., 1997, *Phys. Rew.*, D 56, 535
- Mart nez{G onzalez E. & Sanz J. L., 1990, *MNRAS*, 247, 473
- Mart nez{G onzalez E., Sanz J. L. & Cayon L., 1997, *ApJ*, 484, 1
- Mart nez{G onzalez E., Gallegos J. E., Argueso F., Cayon L. & Sanz J. L., 2002, *MNRAS*, 336, 22

- Mukherjee P., Hobson M. P. & Lasenby A. N., 2000, *MNRAS*, 318, 1157
- Ostriker J. P. & Vishniac E. T., 1986, *ApJ*, 306, L51
- Pando J., Valls-Gabaud D. & Fang L.-Z., 1998, *Phys. Rev. Lett.*, 81, 4568
- Park C. G. 2003, preprint (astro-ph/0307469)
- Peebles P. J. E., 1997, *ApJ*, 483, 1
- Rees M. J. & Sciama D. W., 1968, *Nature*, 517, 611
- Sanz J. L., Argüeso F., Cayon L., Martínez-González E., Barreiro R. B. & Tolatti L., 1999a, *MNRAS*, 309, 672
- Sanz J. L., Barreiro R. B., Cayon L., Martínez-González E., Ruiz G. A., Díaz F. J., Argüeso F., Silk J. & Tolatti L., 1999b, *A&AS*, 140, 99
- Schlegel D. J., Finkbeiner D. P. & Davis M., 1998, *ApJ*, 500, 525
- Seljak U. & Zaldarriaga M., 1996, *ApJ*, 469, 437.
- Spergel D. N. et al., 2003a, *ApJ*, in press
- Stolyarov V., Vielva P., Barreiro R. B., Hobson M. P., Martínez-González E. & Lasenby A. N., 2003, in preparation
- Tegmark M., de Oliveira-Costa A. & Hamilton A. J. S., 2003, preprint (astro-ph/0302496)
- Turok N. & Spergel D. N., 1990, *Phys. Rev. Letters*, 64, 2736
- Tenorio L., Jaffe A. H., Hanany S. & Lineweaver C. H., 1999, *MNRAS*, 310, 823
- Vielva P., Martínez-González E., Cayon L., Diego J. M., Sanz J. L. & Tolatti L., 2001a, *MNRAS*, 326, 181
- Vielva P., Barreiro R. B., Hobson M. P., Martínez-González E., Lasenby A. N., Sanz J. L. & Tolatti L., 2001b, *MNRAS*, 328, 1
- Vielva P., Martínez-González E., Gallegos J. E., Tolatti L. & Sanz J. L., 2003, *MNRAS*, 344, 89

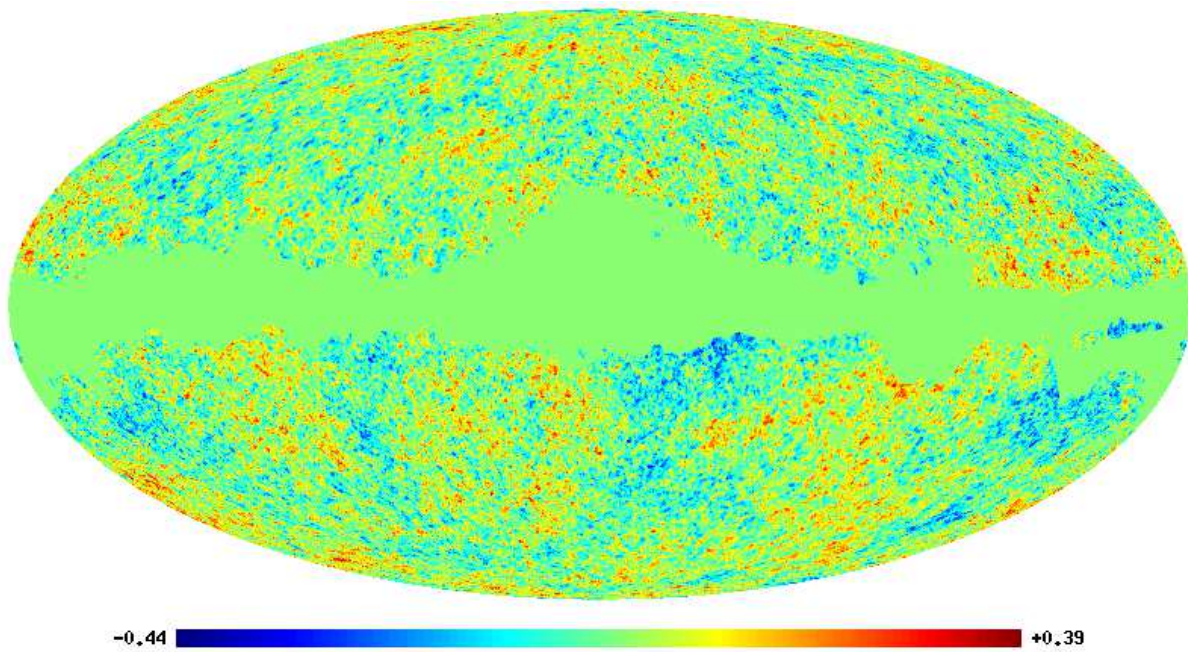


Fig. 1. | Analysed WMAP map at $N_{\text{side}} = 256$ (in mK units). It is a combination of all the receivers in Q-Band, V-Band and W-Band after the foreground correction described in Komatsu (2003). The Kp0 mask is applied and the residual monopole and dipole are subtracted.

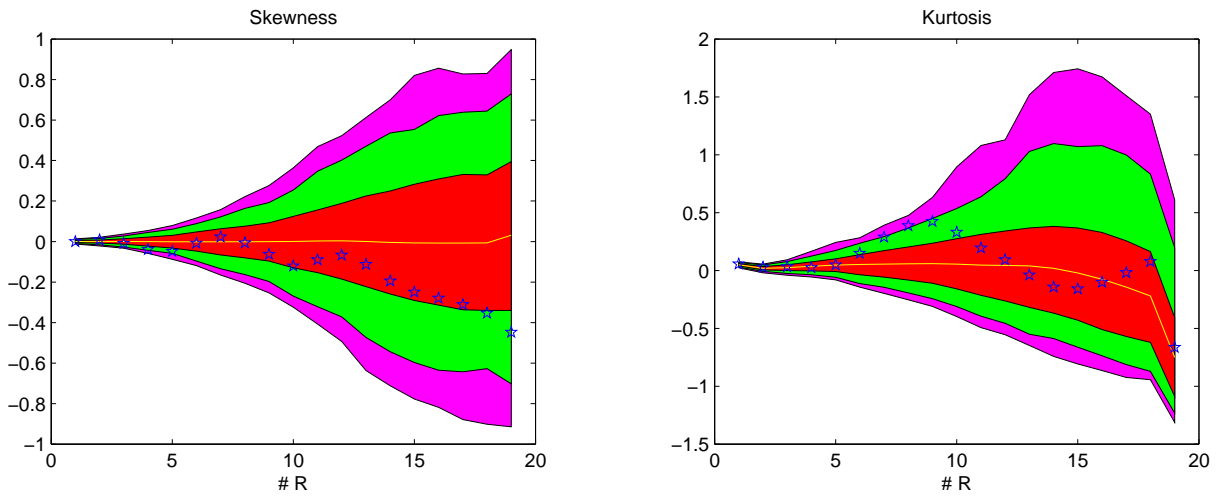


Fig. 2. The skewness ($S(R)$, left panel) and kurtosis ($K(R)$, right panel) curves obtained from the application of the SM HW analysis to the combined WMAP map ($\hat{\Gamma}(x)$) are plotted (blue stars). Confidence regions for the 68% (red, inner), 95% (green, middle) and 99% (magenta, outer) are also plotted, as well as the mean value given by the 1000 simulations (yellow solid line). All the pixels outside the $kp0$ mask have been used in the analysis (see text).

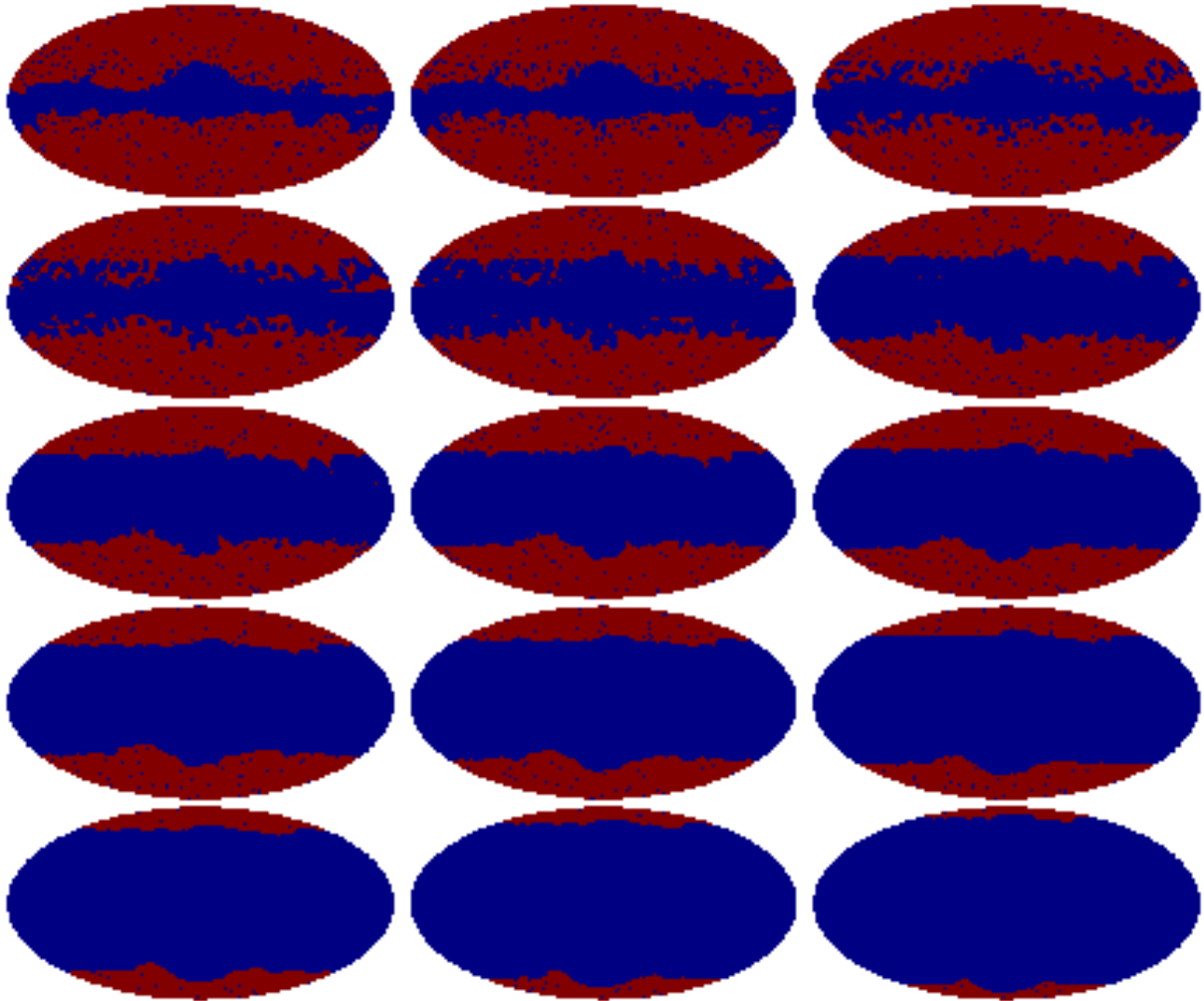


Fig. 3. | Set of exclusion masks ($M(R)$) used in our analysis. This set is defined in order to discard in the SMHW analysis those pixels with a strong k_p0 mask contamination. Since the number of excluded pixels grows with the SMHW scale, there is one exclusion mask per scale R . By introducing the exclusion masks, the analysis improves its efficiency, allowing for a better non-Gaussian detection.

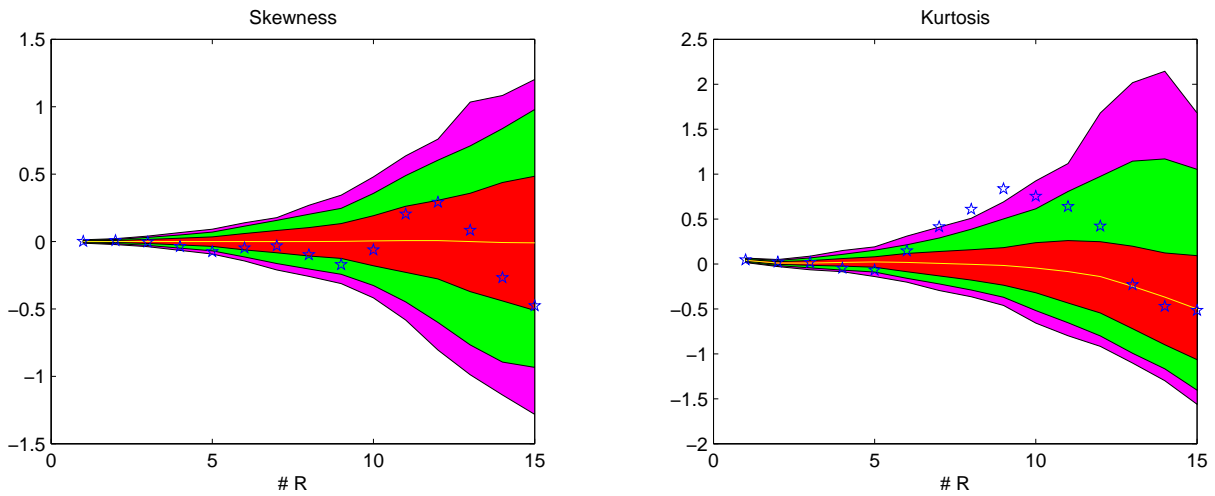


Fig. 4. The skewness ($S(R)$, left panel) and kurtosis ($K(R)$, right panel) curves obtained from the application of the SMHW analysis to the combined WMAP map ($\hat{\Gamma}(x)$) are plotted (blue stars). Confidence regions for the 68% (red, inner), 95% (green, middle) and 99% (magenta, outer) are also plotted, as well as the mean value given by the 1000 simulations (yellow solid line). Only those pixels allowed by the exclusion masks set ($M(R)$) have been used in the analysis (see text).

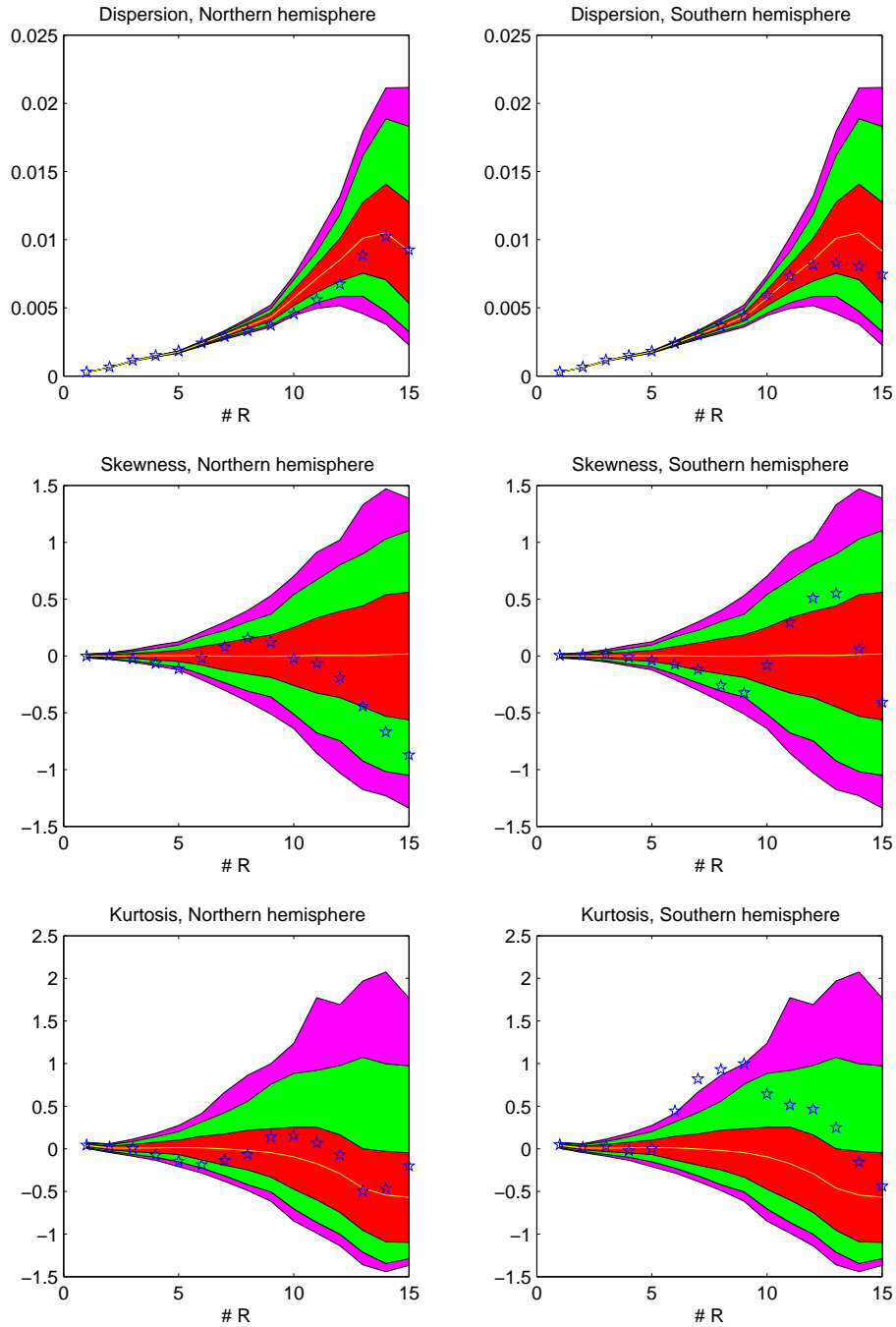


Fig. 5. | The dispersion ($D(R)$, top) skewness ($S(R)$, left middle) and kurtosis ($K(R)$, bottom) curves obtained from the application of the SMHW analysis to the combined WMAP map ($\hat{T}(x)$) are plotted (blue stars). The left column corresponds to the analysis performed only in the northern hemisphere, whereas the analysis of the southern one is in the right column. Confidence regions for the 68% (red, inner), 95% (green, middle) and 99% (magenta, outer) are also plotted, as well as the mean value given by the 1000 simulations (yellow solid line). The exclusion masks set ($M(R)$) have been used in the analysis (see text).

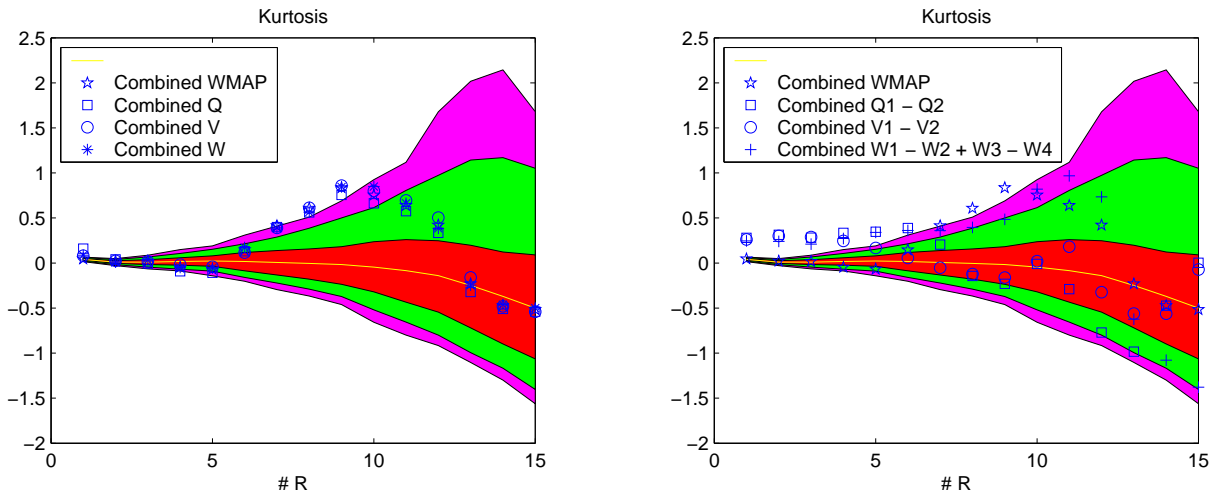


Fig. 6. In the left panel, the kurtosis curve ($K(R)$) obtained from the analysis of each WMAP frequency maps is plotted: Q (blue squares), V (blue circles) and W (blue asterisks). In the right panel, the kurtosis curve ($K(R)$) obtained from the analysis of maps obtained as the subtraction of the receivers at each frequency: the CMB and foreground contribution in these maps is almost negligible. For a better comparison, the kurtosis obtained for the combined WMAP map has been plotted (blue stars) in both panels. As in Figure 4, the confidence regions {68% (red, inner), 95% (green, middle) and 99% (magenta, outer)} for the combined WMAP map ($\hat{T}(x)$) and the mean value given by the 1000 simulations (yellow solid line) are also shown. We have checked that the pattern followed by the kurtosis curve for the combined Q1-Q2 map (in the right panel) can be explained by considering only the noise of that map; we expect that this is also the case for the other subtraction maps: V1-V2 and W1-W2+W3-W4 (although for these later cases the test has not been done because of the very large required CPU time).

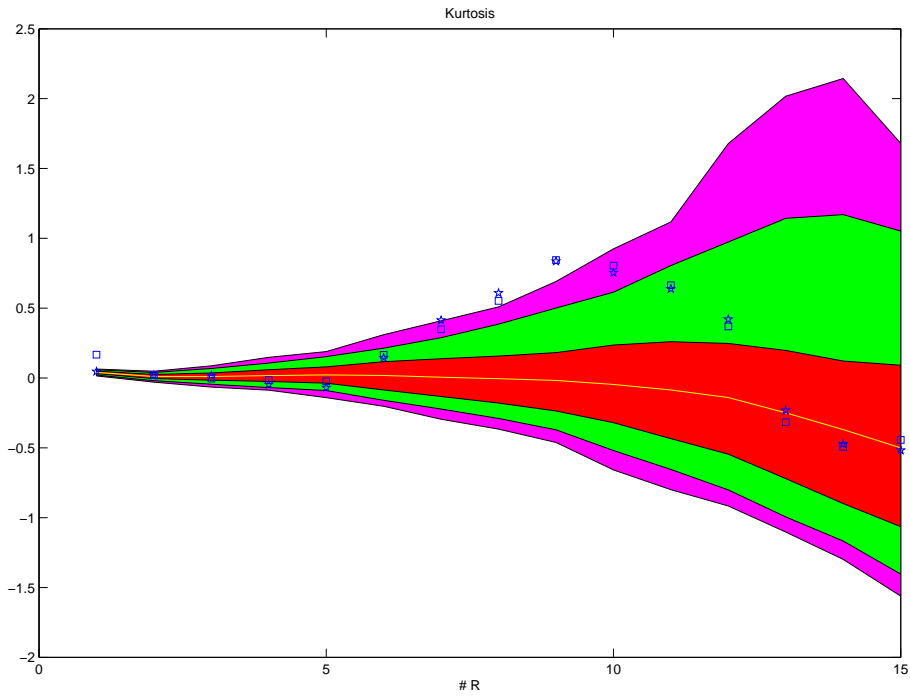


Fig. 7. | The kurtosis curve ($K(R)$) obtained from the combined WMAP map ($\hat{T}(x)$) is plotted (blue stars) together with the one calculated for a CMB map that is obtained after subtracting the K map from the K one taking into account a rough estimation of the synchrotron emission (blue squares). As in Figure 6, the confidence regions { 68% (red, inner), 95% (green, middle) and 99% (magenta, outer) } and the mean value given by the 1000 simulations (yellow solid line) for the combined WMAP map ($\hat{T}(x)$) are also given.

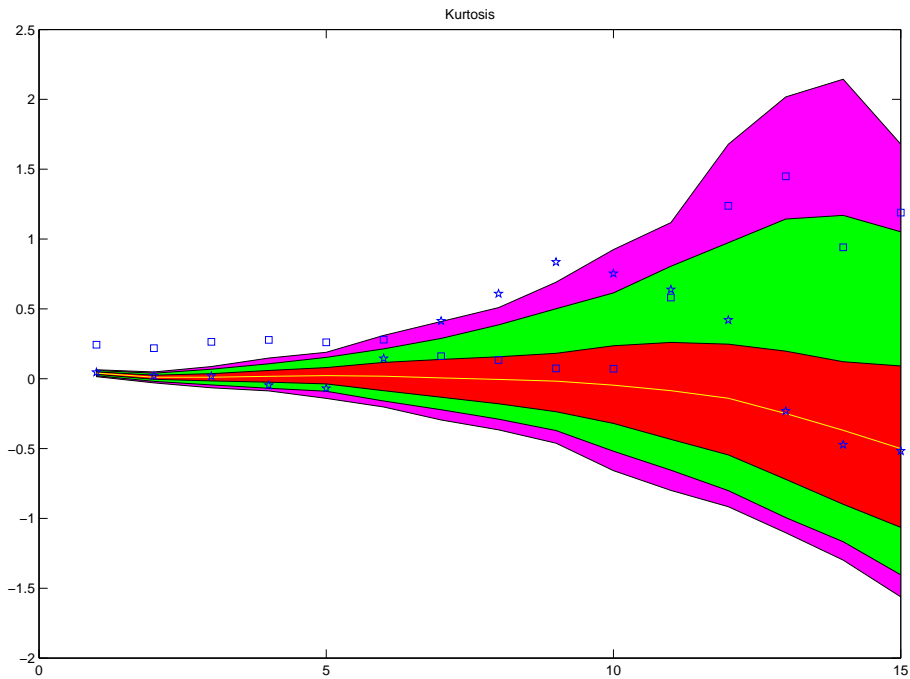


Fig. 8. | The kurtosis curve ($K(R)$) obtained from the combined WMAP map ($\hat{I}(x)$) is plotted (blue stars) together with the one calculated for a CMB map that is obtained after subtracting the Q and V receivers from the W ones (blue squares). This map is almost free of CMB emission. The confidence regions { 68% (red, inner), 95% (green, middle) and 99% (magenta, outer) } and the mean value given by the 1000 simulations (yellow solid line) for the combined WMAP map ($\hat{I}(x)$) are also given for a better comparison. As mentioned in the caption of the Figure 6, we expect that the behaviour for the kurtosis curve of the subtracted map is due to the noise of that map.

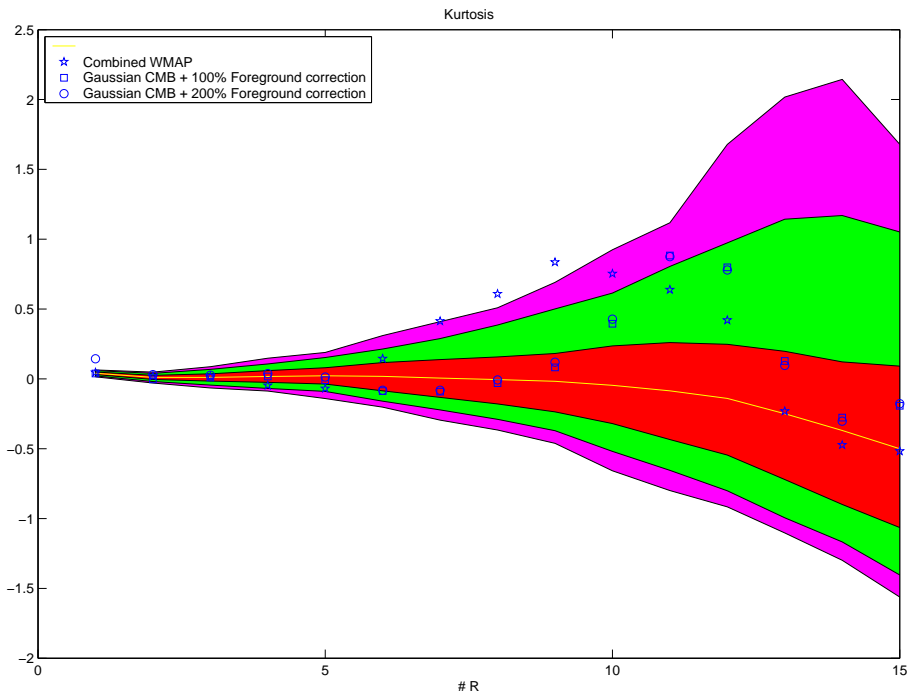


Fig. 9. The kurtosis curves ($K(\hat{T}(x))$) obtained from artificially contaminated CMB Gaussian maps are plotted together with the one calculated for the combined WMAP (blue asterisks). Two different degrees of contamination have been analysed: the one predicted by the WMAP team (blue squares) and twice the previous one (blue circles). The confidence regions { 68% (red, inner), 95% (green, middle) and 99% (magenta, outer) } and the mean value given by the 1000 simulations (yellow solid line) for the combined WMAP map ($\hat{T}(x)$) are also given for a better comparison.

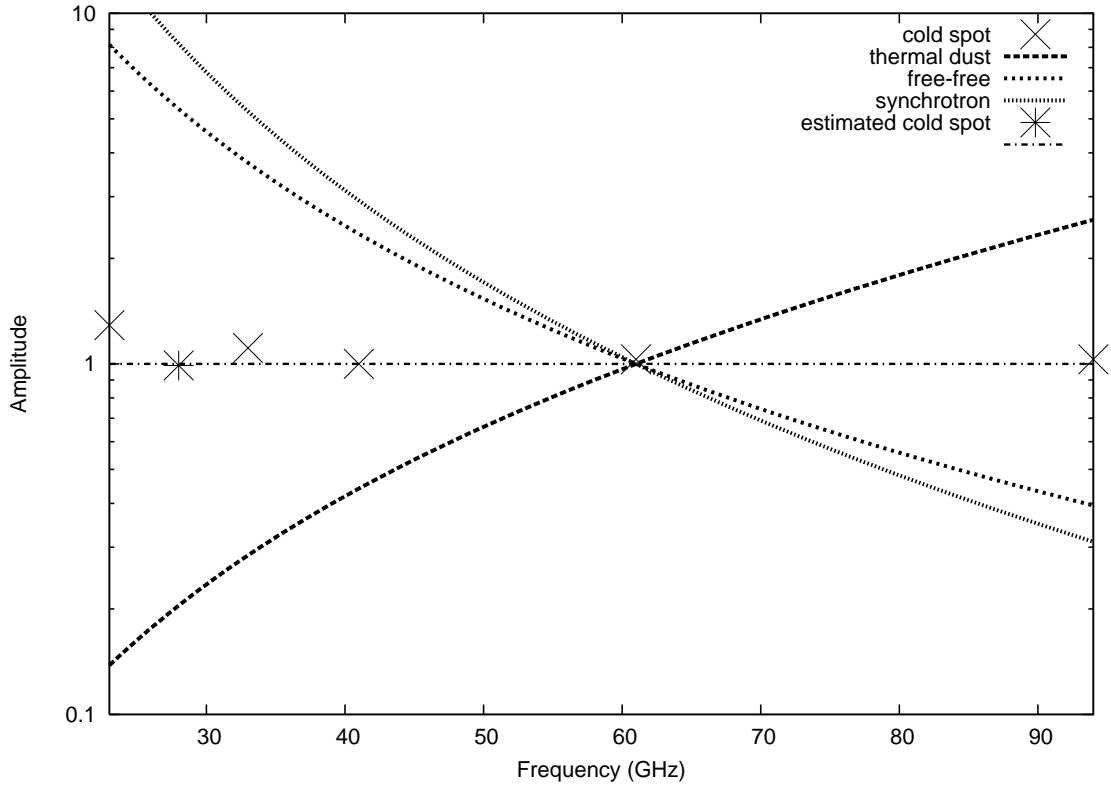


Fig. 11. The mean frequency dependence followed by the 300 most negative SMHW coefficients in the cold spot at $b = 57^\circ; l = 209$ (crosses) is plotted together with the expected frequency dependence for the different foregrounds, at Galactic latitudes $90^\circ < b < 57^\circ$: synchrotron, free-free and thermal dust. The asterisk represents the estimated amplitude of the cold spot, after the K map (corrected by the synchrotron factor, as indicated in the text) is subtracted from the K one. The dot-dashed line has been plotted for comparison with a perfect CMB behaviour. All the amplitudes are normalised to one at the Q-band. Notice that the frequency dependence for the different foregrounds is preserved in wavelet space, due to the linearity of the wavelet convolution.

Kurtosis

